www.MaterialsViews.com

Li-Ion Batteries

SnO_2 Quantum Dots@Graphene Oxide as a High-Rate and Long-Life Anode Material for Lithium-Ion Batteries

Kangning Zhao, Lei Zhang, Rui Xia, Yifan Dong, Wangwang Xu, Chaojiang Niu, Liang He, Mengyu Yan, Longbin Qu, and Liqiang Mai**

Rechargeable lithium-ion batteries (LIBs) have been intensively applied in portable electronic devices and now expanded to the applications in hybrid electric vehicles (HEVs), electric vehicles (EVs), and smart systems.[1–6] In order to meet the demands, special interests have motivated researchers all over the world toward high performance LIBs involving both high energy and power densities.[7–12] Under equilibrium conditions, the total capacity of LIBs can be expressed as [13,14]

$$\text{Total capacity} = \frac{1}{\frac{1}{C_A} + \frac{1}{C_C}} \quad (1)$$

where C_A and C_C are the specific capacities of the anode and cathode materials, respectively. In this way, considering that the specific capacity of current available cathode varies from 140 to 200 mAh g^{-1}, the overall capacity of LIB will witness the most significant improvement if the commercial graphite anode (372 mAh g^{-1}) be replaced by the one with a capacity of around 1000 mAh g^{-1}. This value can be achieved by the alternatives including transition metal oxides, silicon, etc. Thus, it is imperious to develop this kind of anode materials toward high energy density LIBs.

Among them, tin-based materials with their numerous appealing features, including low cost, abundance, environmental benignity, and high theoretical capacity (if both conversion reaction and alloying reaction are taken into account, a theoretical capacity of 1494 mAh g^{-1} is achieved), are regarded as a promising anode for LIBs.[15–23] Generally, tin oxide is regarded to witness a two-step reaction[19]

$$SnO_2 + 4Li^+ + 4e^- = Sn + 2Li_2O \quad (2)$$

$$Sn + 4.4Li^+ + 4.4e^- = Li_{4.4}Sn \quad (3)$$

K. N. Zhao, L. Zhang, R. Xia, Y. F. Dong, C. J. Niu, Dr. L. He, M. Y. Yan, L. B. Qu, Prof. L. Q. Mai
State Key Laboratory of Advanced Technology for Materials Synthesis and Processing
Wuhan University of Technology
Wuhan 430070, China
E-mail: hel@whut.edu.cn; mlq518@whut.edu.cn

W. W. Xu
Department of Mechanical and Industrial Engineering
Louisiana State University
Baton Rouge, LA 70830, USA

DOI: 10.1002/smll.201502183

However, during the alloying process, the large atomic ratio involved results in a 440% increase in the number of atoms and induces huge volume expansions (up to 259%).[19] The huge volume variations result in the repeated expansion and contraction of the lattice along with charge/discharge processes and lead to dislocation, plasticity, cracking, and pulverization of the Sn particles.[16] In this way, the electrical contact between active Sn and conductive additives or the electrode current collector or both is easily lost.[24,25] Moreover, solid electrolyte interface (SEI) layer will continuously and frequently be formed and decomposed on the interface of particles and electrolyte, consuming extra lithium,[26,27] leading to the poor Coulombic efficiency and undesirable capacity fading.

To optimize the cycling stability of electrode materials, the combination of metal oxides and graphene to construct appropriate nanostructures with good structure stability is regarded as an effective method. Graphene with a honeycomb network of sp2 hybridized carbon atoms exhibits excellent electrical conductivity, large surface area, structural flexibility, and chemical stability. However, the simple mechanically mixing metal oxides and graphene usually leads to the agglomeration of nanoparticles and structural instability, especially during the charge–discharge process. Wu et al.[28] designed and fabricated 3D porous graphene network-encapsulated Sn-based architectures preserving the integrity during the long cycling process. Therefore, the construction of stable metal oxides/graphene nanostructures is an effective route to avoid the above problems.[22,29–38] In this regard, it is highly challenging but desirable to develop facile synthesis methodologies for the fabrication of metal oxides nanocrystalline on conducting graphene sheets, particularly for high-rate and long-life LIB applications.

Herein, we report a facile route to synthesize SnO_2 quantum dots@graphene oxide (denoted as SnO_2 QDs@GO) with good dispersion and high mass loading. The formation process involves the oxidation of Sn^{2+} and the reduction of the graphene oxide (GO) sheets. Through in situ reduction process the isolated SnO_2 quantum dots are able to anchor tightly and disperse well on the graphene nanosheets. In this way, the huge volume expansion/contraction associated with lithium insertion/extraction during discharging/charging is effectively released and the structural integrity is well maintained. The unique design is able to offer conductive substrates, facile strain relaxation, and stable SEI layer for fast lithium intercalation/de-intercalation, which yields significant

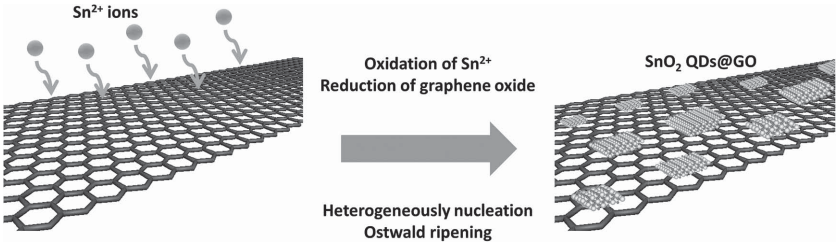

Figure 1. Schematic illustration of the formation process of SnO_2 QDs@GO.

improvements in the cycling stability as well as rate performance for LIBs. The SnO_2 QDs@GO delivers a capacity of 1121 mAh g^{-1} at 100 mA g^{-1} and even at a high current density of 2 A g^{-1}, a capacity retention of 86% (against 2nd capacity) is achieved even after 2000 cycles, largely outperforming previously reported tin-based nanostructure in high-rate cyclability (Table S1, Supporting Information).

The proposed route for the preparation of the SnO_2 QDs@GO is illustrated in **Figure 1**. Graphene oxide (GO) with rich functional groups is applied as a template for the selective heterogeneous nucleation and the growth of SnO_2 QDs. During the hydrothermal process, Sn^{2+} can be in situ oxidized by the rich functional group, then heterogeneously nucleate and grow on the surface of GO. In this way, GO is able to act as both substrate and oxidizing agent. The graphene oxide is reduced to a flake-like hybrid structure composed of numerous SnO_2 QDs. The flake-like hybrid structure is formed by the self-assembly of in situ reduced GO into a 3D architecture by the partial overlapping or coalescing of the flexible graphene during the hydrothermal process.[39] In comparison, SnO_2 particles which are prepared through the same condition without adding graphene show the morphology of aggregated nanoparticles (Figure S1, Supporting Information). The XRD pattern in Figure S2A (Supporting Information) shows that the phase is the same as SnO_2 QDs@GO. Moreover, TG curve in Figure S2B (Supporting Information) shows no weight loss up to 700 °C, indicating no impurity inside. After mixed with GO, the SnO_2/GO composite shows no signs of reduced particle size or enhanced dispersion (Figure S3, Supporting Information). This phenomenon may account for the reasons of the heterogeneous nucleation process on the graphene substrate and the kinetics inhibition of crystal growth.[39]

Figure 2A shows the X-ray diffraction (XRD) patterns of SnO_2 QDs@GO, SnO_2/GO composite, and SnO_2 particles. All the diffraction peaks of SnO_2 QDs@GO, SnO_2/GO composite, and SnO_2 particles are attributed to the tetragonal SnO_2 (JCPDS Card No. 002-1337) with P42/mnm space group. To quantify the content of SnO_2 in the SnO_2@graphene composite, thermogravimetric (TG) measurement was carried out in air (Figure 2B). From the TG curve, SnO_2 QDs@GO shows 12.3% weight loss from 100 to 500 °C which is assigned to combustion of graphene nanosheets in air, forming CO_2. In addition, the weight loss below 100 °C is ≈0.6% which results from the evaporation of water in Figure S4 (Supporting Information). Thus, the weight percentage of SnO_2 in SnO_2 QDs@GO is 87.7% which is among the highest in tin-based oxides/graphene composite reported (Table S1,

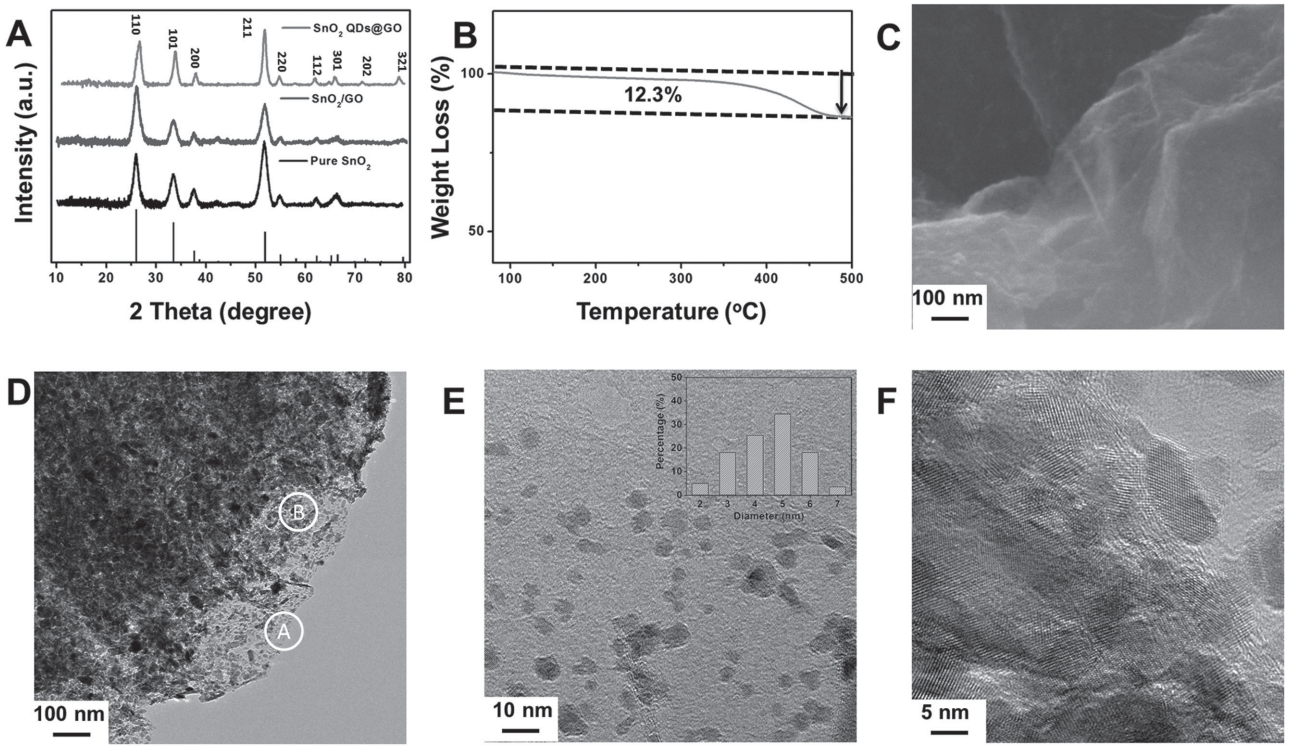

Figure 2. A) XRD patterns of SnO_2 QDs@GO, SnO_2/GO composite, and SnO_2 particles. B) TG curve of SnO_2 QDs@GO at temperature from 100 to 500 °C. C) SEM image, D) Transmission electron microscopy (TEM) image, and E,F) High-resolution TEM (HRTEM) images of SnO_2 QDs@GO.

Supporting Information). The scanning electron microscopy (SEM) image of SnO_2 QDs@GO in Figure 2C reflects that huge sums of small SnO_2 particles are observed on the both sides of the graphene sheets, forming a flake-like hybrid structure. No unattached nanocrystals are observed. A panoramic view in Figure 2D displays the ultrafine SnO_2 particles are homogeneously and densely distributed on the surface of the graphene nanosheets. Additionally, the transparent nature of graphene suggests that it is composed probably of few-layered sheets.[40] In order to identify the structure, two typical domains, A (the edge of graphene) and B (the stacked area) are shown in Figure 2E,F, respectively. Figure 2E shows that on the edge of the graphene nearly all the SnO_2 QDs exhibit uniformly align with the adjacent lattice fringes of 0.34 nm indicating that SnO_2 QDs grow along the [001] direction with exposed (110) surfaces normal to graphene nanosheets (Figure S5, Supporting Information). The preferred orientation may be linked to the oxygen bridging site on SnO_2 (110) plane.[41] The size distribution is shown in the inset of Figure 2E and the sizes of the plates are in range of 2–7 nm. In the stacked area, Figure 2F shows that the SnO_2 plates densely overlaid on the surface of graphene oxide nanosheet, resulting in the high mass loading of SnO_2 (≈87.7%). These results confirm that the SnO_2 QDs distributed uniformly and densely on the graphene oxide nanosheet. In addition, we further investigate the influence of GO functional group on the product. When we change the amount of $KMnO_4$ to be 1.5 g, TEM images in Figure S6 (Supporting Information) show that the SnO_2 nanoparticles are not uniform and randomly distributed. Moreover, the aggregation of the nanoparticles is extremely severe leading to some big particles. In comparison, when the amount of $KMnO_4$ is 3 g, the functional group on the GO nanosheet is richer, GO nanosheet is able to provide more active sites for nucleation. In this way the in situ reduction is realized and the SnO_2 QDs@GO composite is obtained.

The presence of graphene is determined by Fourier transform infrared spectroscopy (FT-IR) in **Figure 3**A and in spectra of the SnO_2 QDs@GO, SnO_2/GO composite, SnO_2 particles, and GO, the peak at 1628 cm^{-1} can be attributed to O-H bending vibrations. Carboxyl and epoxy functional groups are detected at ≈1732, 1225, and 1052 cm^{-1}, respectively.[20] The peaks at 1732 cm^{-1} are assigned to the carboxyl group while the peaks at 1225 and 1052 cm^{-1} are belonged to carboxyl group and epoxy functional groups. A broad peak at 621 cm^{-1} can be assigned to the vibration of Sn-O-Sn, confirming the presence of SnO_2 in SnO_2 QDs@GO, SnO_2/GO composite. No characteristic peaks of GO are found in the SnO_2 spectrum, indicating the existence of graphene in the SnO_2 QDs@GO and SnO_2/GO composite. The property of graphene in SnO_2 QDs@GO, SnO_2/GO composite, and GO is determined by Raman spectra in Figure 3B. The peak at ≈1581 cm^{-1} (G band) corresponds to the E2g mode of graphite, which is related to the vibration of sp2 bonded carbon atoms in a 2D hexagonal lattice. The peak at ≈1346 cm^{-1} (D band) is an indication of defects associated with vacancies, grain boundaries, and amorphous carbon species.[40] The intensity ratio (I_D/I_G) of the D band to the G band is related to the extent of disorder degree and average size of the sp2 domains. From Figure 3B, the I_D/I_G ratios of SnO_2 QDs@GO, SnO_2/GO composite, and GO are 1.14, 0.97, and 1.07, respectively. The increased I_D/I_G ratio of SnO_2 QDs@GO indicates the partially reduction of GO by Sn^{2+} as well as the anchoring of nanoparticles on the graphene nanosheets through in situ reduction process and the decreased I_D/I_G ratio of SnO_2/GO

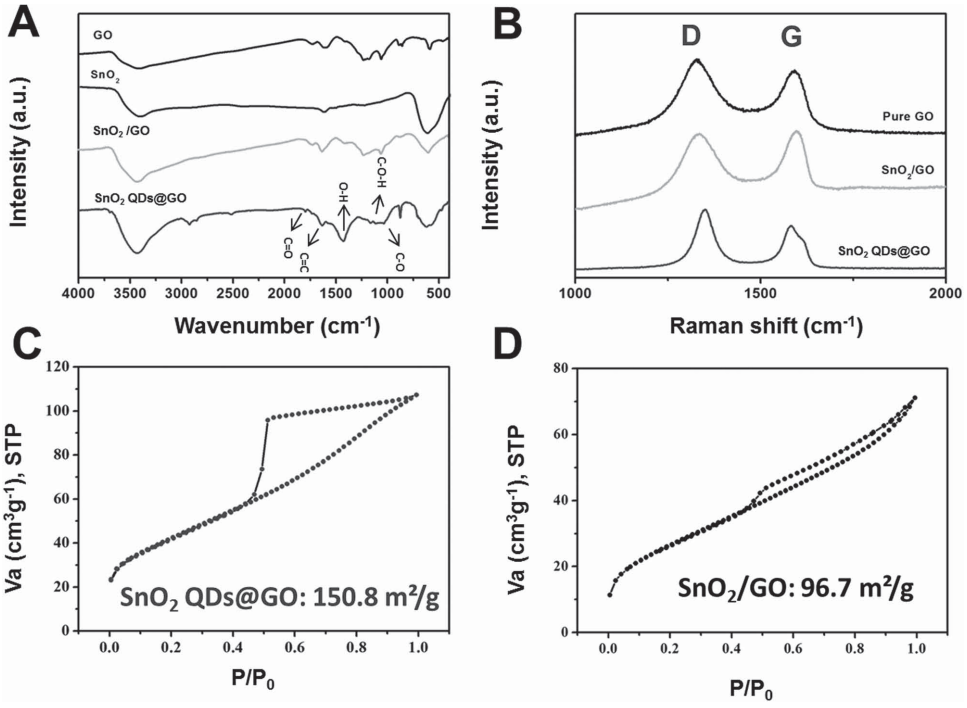

Figure 3. A) FT-IR spectra of SnO_2 QDs@GO, SnO_2/GO composite, SnO_2 particles, and graphene oxide. B) Raman spectra of SnO_2 QDs@GO, SnO_2/GO composite, and graphene oxide. Nitrogen adsorption/desorption isotherms of C) SnO_2 QDs@GO and D) SnO_2/GO.

composite is accounted for the agglomeration of graphene oxide nanosheet.[40] The nitrogen adsorption/desorption isotherms of SnO_2 QDs@GO, SnO_2/GO composite, and SnO_2 particles were also studied. The specific surface area of SnO_2 QDs@GO measured by the BET method is 150.8 m^2 g^{-1}, which is the largest among those of SnO_2/GO composite (96.7 m^2 g^{-1}) and SnO_2 particles (60.7 m^2 g^{-1}, Figure S7, Supporting Information), implying the highly dispersion of SnO_2 nanocrystals decorated on graphene nanosheets.[42] Moreover, no obvious pores are observed in the pore size distribution for SnO_2 QDs@GO and SnO_2/GO composite in Figure S8 (Supporting Information).

The electrochemical performance of the SnO_2 QDs@GO, SnO_2/GO composite, and SnO_2 nanoparticles is evaluated for lithium storage by using 1 M $LiPF_6$ in ethyl carbonate/diethyl carbonate (EC/DEC) as the electrolyte and lithium metal as counter electrode. The deep galvanostatic cycling between 0.01 and 3 V at 100 mA g^{-1} is carried out (**Figure 4**A). Noticeably, all the three samples show the capacity decay during the initial cycle. The initial irreversible capacity is because of the following reasons. First, the frequent formation of solid electrolyte interphase (SEI) layer trapped lithium ions. Second, the conversion reaction of SnO_2 is partially reversible.[19,20] During the second discharge process, the SnO_2 QDs@GO delivers a capacity of 1107 mAh g^{-1}, which is higher than those of SnO_2/GO composite (676 mAh g^{-1}) and SnO_2 particles (924 mAh g^{-1}) (Figure 4B). More specifically, after 100 cycles, a capacity of 1121 mAh g^{-1} is well retained indicating that the minor capacity increase is observed. Thus, in order to investigate the high-rate cycling stability, a high current density of 2 A g^{-1} is applied and the 2nd capacity of SnO_2 QDs@GO can reach 553 mAh g^{-1} (Figure 4C). Even after 2000 cycles the capacity of 477 mAh g^{-1} is retained, corresponding to the capacity retention of 86%, which, to the best of our knowledge, is the longest cycling performance of tin-based electrodes reported. The Coulombic efficiencies after the initial 3 cycles remain above 98%, indicating that the structure of the electrode and the SEI layer on the surface of the electrode is

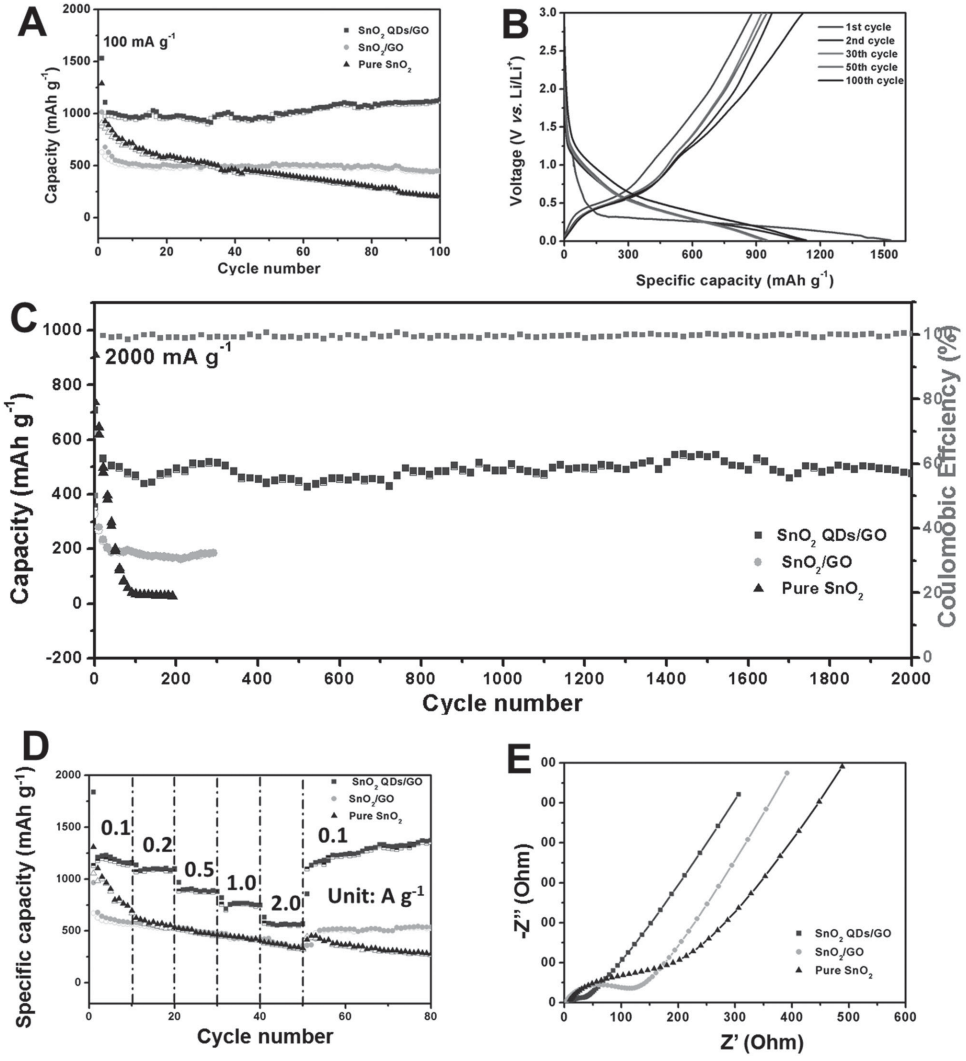

Figure 4. A) Cycling performance of SnO_2 QDs@GO, SnO_2/GO composite, and SnO_2 particles at 100 mA g^{-1}. B) Galvanostatic charge/discharge profiles of the initial two cycles, 30th cycles, 50th cycles, and 100th cycles of SnO_2 QDs@GO at 100 mA g^{-1}. C) High-rate cycling performance and the corresponding Coulombic efficiency of SnO_2 QDs@GO, SnO_2/GO composite, and SnO_2 particles. D) Rate capability of SnO_2 QDs@GO, SnO_2/GO composite, and SnO_2 particles. E) Impedance responses of SnO_2 QDs@GO, SnO_2/GO composite, and SnO_2 particles.

stable in the following cycles. To evaluate the rate capability, different current densities ranging from 0.1, 0.2, 0.5, 1, to 2 A g^{-1} are applied (Figure 4D). Remarkably, even at a high current density of 2 A g^{-1}, the capacity still retains 566 mAh g^{-1}, showing outstanding rate capability. The capacity of the SnO_2/GO composite and SnO_2 particles quickly dropped to below the theoretical capacity of commercialized graphite (372 mAh g^{-1}). When the current density returns to 100 mA g^{-1}, the capacity of SnO_2 QDs@GO still retains 1130 mAh g^{-1}. The corresponding capacity recovery is 97%, indicating that the structure is stable even suffering from the high current density, outperforming the SnO_2/GO composite (89%) and SnO_2 particles (41%). Furthermore, full cells using $LiFePO_4$ as cathode were characterized by galvanostatic cycling with potential limitation (1.5–3.7 V) at 1.0 A g^{-1}. In addition, the capacity is calculated based on the mass of anode materials (SnO_2 QDs@GO electrode). The capacity of anode at 1.0 A g^{-1} is 761 mAh g^{-1} which is ≈5.1 times higher than that of cathode. Thus, in order to match the capacity of cathode and anode, the mass ratio should be 5.1:1.0. The SnO_2 QDs@GO electrode shows the high reversible capacity of 516 mAh g^{-1} at 1 A g^{-1} which is much higher than that of commercial graphite in Figure S10 (Supporting Information). Figure S11 (Supporting Information) is a digital image of a light-emitting-diode (LED) lighting by the SnO_2 QDs@GO/$LiFePO_4$ lithium ion battery. These results indicate the promising potential of SnO_2 QDs@GO as high energy density anode for lithium ion battery.

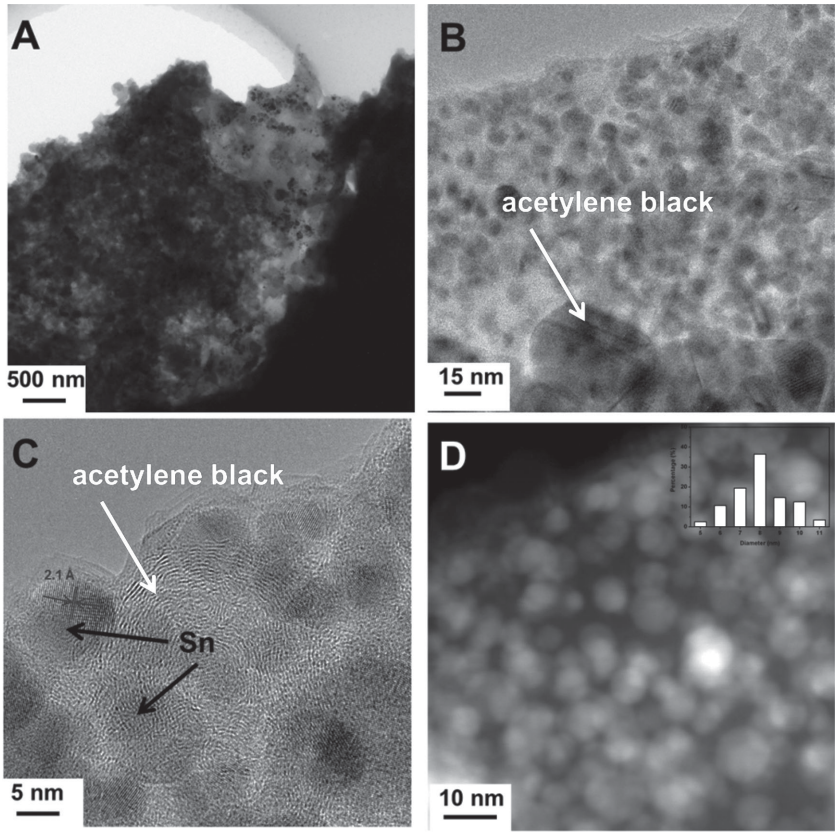

Figure 5. A–C) TEM images of SnO_2 QDs@GO after 100 cycles. D) The dark field TEM image of SnO_2 QDs@GO after 100 cycles.

To provide further insights, the electrochemical impedance spectrum shows a compressed semicircle from the high to medium frequency range of each spectrum, and a line inclined at ≈45° in the low-frequency range (Figure 4E).[37,38] The compressed semicircle describes the charge transfer resistance (R_{ct}) for these electrodes and the inclined line is considered as Warburg impedance (Z_W). In the equivalent circuit (Figure S12, Supporting Information), R_1 represents the Ohmic resistance of the electrode system, including the electrolyte and the cell components. R_2 and R_3 represent the resistance related to SEI and the charge transfer, respectively. CPE_1, CPE_2 and Z_w are the capacitance related to SEI, the double layer, and the Warburg impedance, respectively. The smaller diameter of the semicircle for the SnO_2 QDs@GO electrode indicates an enhanced conductance of Li^+ when compared to the SnO_2/GO composite and SnO_2 particles (Figure S13, Supporting Information). This result suggests that SnO_2 QDs@GO holds enhanced kinetics for Li ion insertion/extraction.

The ex situ TEM images of SnO_2 QDs@GO after 100 cycles is presented in **Figure 5**. A paramonic view in Figure 5A shows that huge sums of acetylene black is observed on the graphene oxide nanosheet. Thus in order to obtain clear view of the sample, the edge of graphene is presented. The magnified TEM image in Figure 5B shows that there still are many small particles on the surface of the graphene oxide nanosheet indicating the excellent structural integrity. The magnified HRTEM in Figure 5C shows that the lattice fringes of 2.1 Å indicating that the particles are tin and correspond to the (220) plane. This result demonstrates that the structural integrity is well maintained even after 100 cycles. Moreover, in order to obtain the size distribution of the particle, the dark field TEM image is carried out. The size distribution of the particle is shown in Figure 5D and the average size is 8 nm which is 1.6 times higher than that before cycling. The inevitable volume variation during discharging leads to the expansion of SnO_2 nanocrystals in size. These results strongly indicates that despite the increase in particle size, SnO_2 QDs@GO can well maintain the mechanical integrity as well as electronic connection between the SnO_2 quantum dot and the graphene oxide nanosheet and buffer the internal stress upon charging/discharging.

The outstanding electrochemical performance can be attributed to the aspects below. First, the higher surface area of SnO_2 QDs@GO allows for greater electrolyte wetting and lithium-ion access, providing more sites to the solvated Li^+ for charge transfer processes, which is reflected as the enhanced conductance at the electrolyte/electrode interface. Second, graphene sheet is able to serve as an elastic

conductive network and the ultrafine SnO_2 quantum dots on conductive graphene substrates. Thus, this structure can offer not only large numbers of accessible active sites for lithium-ion insertion but also short diffusion path length for lithium ions, which are beneficial for high capacity and rate capability. Meanwhile, due to quantum size effect, the isolated SnO_2 quantum dots anchoring tightly and dispersed well on the graphene nanosheets can effectively release the huge volume expansion/contraction associated with lithium insertion/extraction during discharging/charging, which is beneficial for cycling stability.

In conclusion, we develop a facile approach for preparing SnO_2 QDs@GO with good dispersion and high mass loading through in situ reduction of GO and oxidation of Sn^{2+}. The SnO_2 QDs@GO exhibits promising performance as anode for LIB in terms of high capacity (a capacity of 1121 mAh g^{-1} at current density of 100 m A g^{-1}) and outstanding high-rate cycling stability (a capacity retention of 86% at current density of 2 A g^{-1} after 2000 cycles against 2nd cycle). These results demonstrate this kind of unique design is a successful combination of high conductive graphene sheets and ultrafine quantum dots. The good dispersion and high mass loading of SnO_2 quantum dots on the graphene sheet can provide a great deal of active sites, which in return provides high lithium storage capacity. Meanwhile, the voids between each quantum dot are able to provide space for the volume variation for lithium intercalation/deintercalation and inhibit the aggregation of each particle. Moreover, the conductive graphene sheet endows each quantum dot with sufficient electrical conductivity and the quantum dots offer shortened lithium diffusion length, which result in the enhanced kinetics and thus, high-rate cycling stability is achieved. The desirable confinement of SnO_2 quantum dots in graphene sheets would be very helpful in boosting the electrochemical performance of other nanomaterials.

Experimental Section

Materials Synthesis

Preparation of the SnO_2 QDs@GO: The graphene oxide (GO) solution was synthesized by the modified hammer's method. In a typical systhesis, 0.7 g of $SnCl_2{\cdot}2H_2O$ and a proper amout of hydrochloric acid was mixed with 40 mL deinonized water forming an aqueous solution. Then 5 mL of GO solution (1.5 mg mL^{-1}) is added into the the suspension. After stirring for 15 min, the suspension was transferred into autoclave which had been set to 200 °C for 12 h. After cooled down to room temperature, the precipitation was then collected and washed with DI water and alcohol for several times. After drying for 12 h at 60 °C, the SnO_2 QDs@GO was obtained. As a comparison, the SnO_2 particles were prepared through the same procedure above without adding graphene and the SnO_2/GO composite was obtained by simply mixing SnO_2 particles and graphene at mass ratio of 88:12.

Material characterization: XRD data of samples were collected with a D8 Advance X-ray diffractometer with area detector, using Cu Kα radiation (λ = 1.5418 Å) in a 2θ range from 10° to 80°. The microstructures were observed by field-emission scanning electron microscopy (FESEM) (JEOL-7100F), and transmission electron microscopy and high-resolution transmission electron microscopy (HRTEM) (JEM-2100F). FT-IR spectra were obtained using a Nexus system. Brunauer Emmet-Teller (BET) surface areas were measured by using Tristar II 3020 instrument. Raman spectra were acquired using a Renishaw RM-1000 laser Raman microscopy system.

Electrochemical characterization: The electrochemical properties were characterized by assembly of CR2016-type coin cells with lithium metal foil as the anode in a glovebox filled with pure argon gas. The cathode electrodes were composed of 70% active material, 20% acetylene black, and 10% sodium alginate binder. A solution (1 M) of $LiPF_6$ in EC/DMC (1:1 vol/vol) was used as the electrolyte. Copper foil is used as collector for the coating. The cells were aged for 12 h before charge/discharge process to ensure full filteration of the electrolyte into the electrodes. The capacity was caculated based on the total mass of the composite. The mass loading of each electrode is 1.4–2.1 mg cm^{-2}. Galvanostatic charge/discharge measurement was performed by a multichannel battery testing system (LAND CT2001A), cyclic voltammetry (0.01–3 V) was performed using an electrochemical workstation (CHI 760S), and electrochemical impedance spectroscopy (EIS) was tested with an Autolab Potentiostat Galvanostat (PGSTAT302N). The EIS is carried out at frequency range from 0.1 to 10000 Hz at open circuit potential before cycling to avoid the influence of Li metal. All the measurements were carried out at room temperature. In order to prepare the TEM images after cycling, the electrode was taken out of the disassembled cell and soaked immediately in acetone for 24 h for washing the residue of electrolytes. The samples after cycling were detached using sonicator and dispersed in the alcohol to form suspension. The smart grid was dipped in the suspension for TEM characterization. In assembly of full cell, we used commercialized $LiFePO_4$ which is purchased from Tianjin STL Energy Technology Co., Ltd. as cathode.

Supporting Information

Supporting Information is available from the Wiley Online Library or from the author.

Acknowledgements

K.N.Z., L.Z., and R.X. contributed equally to this work. This work was supported by the National Basic Research Program of China (Grant Nos. 2013CB934103 and 2012CB933003), the International Science and Technology Cooperation Program of China (Grant No. 2013DFA50840), the National Natural Science Foundation of China (Grant Nos. 51302203, 51272197, and 515210001), the National Science Fund for Distinguished Young Scholars (Grant No. 51425204), the Hubei Science Fund for Distinguished Young Scholars (Grant No. 2014CFA035), the Fundamental Research Funds for the Central Universities (Grant Nos. 143201003, 2014-VII-007, 2014-YB-001, 2014-YB-002, and 2014-ZY-016), and the Students Innovation and Entrepreneurship Training Program (Grant No.

20141049701008). The authors are deeply thankful to Prof. C. M. Lieber of Harvard University and Prof. Jun Liu of Pacific Northwest National Laboratory for their stimulating discussions and kind help.

[1] S. Chu, A. Majumdar, *Nature* **2012**, *488*, 294.
[2] D. Larcher, J.-M. Tarascon, *Nat. Chem.* **2015**, *7*, 11.
[3] L. Mai, X. Tian, X. Xu, L. Chang, L. Xu, *Chem. Rev.* **2014**, *114*, 11828.
[4] P. L. Taberna, S. Mitra, P. Poizot, P. Simon, J. M. Tarascon, *Nat. Mater.* **2006**, *5*, 567.
[5] Y. F. Dong, S. Li, K. N. Zhao, C. H. Han, W. Chen, B. L. Wang, L. Wang, B. Xu, Q. L. Wei, L. Zhang, X. Xu, L. Q. Mai, *Energy Environ. Sci.* **2015**, *8*, 1267.
[6] C. Niu, J. Meng, X. Wang, C. Han, M. Yan, K. Zhao, X. Xu, W. Ren, Y. Zhao, L. Xu, Q. Zhang, D. Zhao, L. Mai, *Nat. Commun.* **2015**, *6*, 7402.
[7] A. R. Armstrong, C. Lyness, P. M. Panchmatia, M. S. Islam, P. G. Bruce, *Nat. Mater.* **2011**, *10*, 7.
[8] K. G. Gallagher, S. Goebel, T. Greszler, M. Mathias, W. Oelerich, D. Eroglu, V. Srinivasan, *Energy Environ. Sci.* **2014**, *7*, 1555.
[9] Z. Hu, Z. Zhu, F. Cheng, K. Zhang, J. Wang, C. Chen, J. Chen, *Energy Environ. Sci.* **2014**, *8*, 7.
[10] A. Magasinski, P. Dixon, B. Hertzberg, A. Kvit, J. Ayala, G. Yushin, *Nat. Mater.* **2010**, *9*, 6.
[11] C. Wang, H. Wu, Z. Chen, M. T. McDowell, Y. Cui, Z. Bao, *Nat. Chem.* **2013**, *5*, 7.
[12] S. Xin, Y.-G. Guo, L.-J. Wan, *Acc. Chem. Res.* **2012**, *45*, 1759.
[13] U. Kasavajjula, C. Wang, A. J. Appleby, *J. Power Sources* **2007**, *163*, 1003.
[14] M. Yoshio, T. Tsumura, N. Dimov, *J. Power Sources* **2005**, *146*, 10.
[15] C. Guan, X. Wang, Q. Zhang, Z. Fan, H. Zhang, H. J. Fan, *Nano Lett.* **2014**, *14*, 4852.
[16] J. Y. Huang, L. Zhong, C. M. Wang, J. P. Sullivan, W. Xu, L. Q. Zhang, S. X. Mao, N. S. Hudak, X. H. Liu, A. Subramanian, H. Fan, L. Qi, A. Kushima, J. Li, *Science* **2010**, *330*, 6.
[17] J. Liang, X.-Y. Yu, H. Zhou, H. B. Wu, S. Ding, X. W. D. Lou, *Angew. Chem., Int. Ed.* **2014**, *53*, 12803.
[18] L. Zhang, H. B. Wu, B. Liu, X. W. Lou, *Energy Environ. Sci.* **2014**, *7*, 1013.
[19] L. Zhang, K. Zhao, W. Xu, Y. Dong, R. L. Xia, F. Liu, L. He, Q. Wei, M. Yan, L. Mai, *Phys. Chem. Chem. Phys.* **2015**, *17*, 5.
[20] X. Zhou, L.-J. Wan, Y.-G. Guo, *Adv. Mater.* **2013**, *25*, 2152.
[21] V. Raju, X. Wang, W. Luo, X. Ji, *Chem. – A Eur. J.* **2014**, *20*, 7686.
[22] H. Song, N. Li, H. Cui, C. Wang, *J. Mater. Chem. A* **2013**, *1*, 7558.
[23] N. Yesibolati, M. Shahid, W. Chen, M. N. Hedhili, M. C. Reuter, F. M. Ross, H. N. Alshareef, *Small* **2014**, *10*, 2849.
[24] T. Jaumann, M. Herklotz, M. Klose, K. Pinkert, S. Oswald, J. Eckert, L. Giebeler, *Chem. Mater.* **2015**, *27*, 37.
[25] L. Wang, D. Wang, Z. Dong, F. Zhang, J. Jin, *Nano Lett.* **2013**, *12*, 1711.
[26] W. Xu, K. Zhao, C. Niu, L. Zhang, Z. Cai, C. Han, L. He, T. Shen, M. Yan, L. Qu, L. Mai, *Nano Energy* **2014**, *8*, 196.
[27] Y. Yao, N. Liu, M. T. McDowell, M. Pasta, Y. Cui, *Energy Environ. Sci.* **2012**, *5*, 7927.
[28] C. Wu, J. Maier, Y. Yu, *Adv. Funct. Mater.* **2015**, *25*, 3488.
[29] C. Han, M. Yan, L. Mai, X. Tian, L. Xu, X. Xu, Q. An, Y. Zhao, X. Ma, J. Xie, *Nano Energy* **2013**, *2*, 916.
[30] J. Liu, K. Song, C. Zhu, C.-C. Chen, P. A. V. Aken, J. Maier, Y. Yu, *ACS Nano* **2014**, *8*, 9.
[31] R. Mo, Z. Lei, K. Sun, D. Rooney, *Adv. Mater.* **2014**, *26*, 2084.
[32] C. Peng, B. Chen, Y. Qin, S. Yang, C. Li, Y. Zuo, S. Liu, J. Yang, *ACS Nano* **2010**, *6*, 8.
[33] H. Song, G. Yang, H. Cui, C. Wang, *Nano Energy* **2014**, *3*, 16.
[34] X. Xu, J. Zhuang, X. Wang, *J. Am. Chem. Soc.* **2008**, *13*, 9.
[35] G. Zhang, S. Hou, H. Zhang, W. Zeng, F. Yan, C. C. Li, H. Duan, *Adv. Mater.* **2015**, *27*, 2400.
[36] Q. Zhao, X. Hu, K. Zhang, N. Zhang, Y. Hu, J. Chen, *Nano Lett.* **2015**, *15*, 721.
[37] C. Zhu, X. Mu, P. A. van Aken, Y. Yu, J. Maier, *Angew. Chem., Int. Ed.* **2014**, *53*, 2152.
[38] Z. Zhu, S. Wang, J. Du, Q. Jin, T. Zhang, F. Cheng, J. Chen, *Nano Lett.* **2014**, *14*, 153.
[39] W. Wang, L. Hu, J. Ge, Z. Hu, H. Sun, H. Sun, H. Zhang, H. Zhu, S. Jiao, *Chem. Mater.* **2014**, *26*, 3721.
[40] L. Liu, M. An, P. Yang, J. Zhang, *Sci. Rep.* **2015**, *5*, 9055.
[41] J. Yue, X. Jiang, A. Yu, *J. Phys. Chem. C* **2013**, *117*, 9962.
[42] V. Etacheri, G. A. Seisenbaeva, J. Caruthers, G. Daniel, J.-M. Nedelec, V. G. Kessler, V. G. Pol, *Adv. Energy Mater.* **2015**, *5*, 1401289.

Received: July 22, 2015
Revised: October 30, 2015
Published online: December 17, 2015